Development of a dynamic ice penetration model for runway de-icing products through performance experimental characterization

Claire Charpentier (claire.charpentier1@uqac.ca), Jean-Denis Brassard (jdbrassa@uqac.ca), Gelareh Momen (gelareh_momen@uqac.ca), and Jean Perron (j1perron@uqac.ca)

Abstract

During winter, the clear runway concept is crucial to airports for maintaining passenger and employee safety. Research can optimize de-icing product application rates, thereby reducing costs and environmental impact. Currently, three aerospace standards exist for evaluating the performance of runway de-icing products. These comparative tests—ice melting, ice undercutting, and ice penetration tests—are carried out jointly in a systematic way and indicate whether a runway de-icing product is effective in actively reducing the presence of ice. Here we present a numerical model for the ice penetration method, for fluid runway de-icing product, with the goal of deepening the knowledge in this field. We apply a series of laboratory-based tests to measure the performance of runway de-icing products, and develop a new model to analyze the behavior of each product. The principal observation is that the product is more effective at 1 minute and effectiveness decreases following an inverse logarithmic curve trend to 30 minutes. Through modeling, we observe that the dominant mode of heat transfer is natural laminar convection, and the model predicts a uniform melt length for the entire tube section. Thus, simplified ice penetration modeling using AS6211 can acceptably predict the rate of ice penetration as a function of time (mm/min), with the modelling confirmed by our experimental results. The future application of our simplified model to other existing de-icing fluid characterization test methods could identify the effects of

diluted or undiluted solid runway de-icing products on ice penetration rates and ultimately on spreading rates.

Nomenclature

A: interchange area

C: concentration

Cp: specific heat

CV1: control volume of ice

CV2: control volume of RDP (KAC)

CV3: control volume of brine

D: width

E_{cv}: energy of Control Volume

E_{in}: energy inside

E_{out}: energy outside

$\dot{E}$: variation of energy as a function of time

g: gravitational acceleration due to Earth

Gr: Grashoff number

h: heat coefficient

H_{sl}: latent heat of ice fusion

k: thermal conductivity

L: lengh

m_i: mass of pure RDP

m_1: mass of ice

m_2: mass of RDP 50 w/w (KAC)

m_3: mass of brine

$\dot{m}$: mass flow

Nu: Nusselt Number

Pr: Prandtl number

q: thermal flow

Ra: Rayleigh number

Ra_c: critical Rayleigh number

RDP: runway de-icing product

r_o: outside radius of tube

r_i: inside radius of tube

t: time

T: temperature

T_{di}: melting temperature of fluid

T_{min}: minimal temperature

T_1: temperature of ice

T_2: temperature of RDP 50 w/w (KAC)

T_3: temperature of brine

T_4: temperature of sample tube

T_0: temperature of climatic chamber

$\dot{T}$: variation of temperature as a function of time

x_1: depth of ice

x_2: depth of RDP (KAC)

x_3: depth of brine

$\dot{x}$: variation of the depth as a function of time

α: thermal diffusivity

β: thermal expansion

ΔE_{tot}: difference of total energy

ρ: density

ν: kinematic viscosity

1. Introduction

During airport winter maintenance operation in northern countries such as Canada and United States, thousands of kilograms of de-icing products, in both fluid and solid form, are applied to airport runways to make the winter contaminant more easily removed using mechanical tools and thus promote safe aircraft take-offs and landings. Most of these adverse conditions involve what is commonly known as atmospheric icing, which includes freezing rain, wet or dry snow, ice pellets, freezing drizzle precipitation, and frost, resulting from the deposition of water vapor directly into ice crystals [1]. These weather events can result in hazardous runway conditions that increase the risk to users [2] [3]. Although these winter conditions are recurrent and, in some cases, worsen from year to year, to date very little attention has been paid to evaluating the performance and determining the optimal amounts of de-icing and anti-icing products to apply to runways. Each product supplier specifies application rates and the duration of effectiveness on the basis of their own experiences and knowledge.

Many aircraft accidents are attributable to poor runway conditions [4]. The presence of water, ice, or snow [3] on runways has been identified as a key factor leading to aircraft accidents between 2010 and 2019 [5]. Among them, on February 8, 2019, an aircraft ran off the runway at Saguenay–Bagotville (Québec) airport after landing [6]. A total of 42 passengers and 3 crew members were on board, but fortunately there were no injuries. Runway excursion is classified as one of the two most important risk areas in the aviation industry [7-9], and the risk of an icy runway in Canada is high [10, 11]. Most of these recorded accidents had significant property damage consequences [12]. Northern winter conditions favor a greater frequency of accidents and therefore impact negatively the airports [13].

To counter runway icing, airport operators apply significant quantities of de-icing products onto the runways. Most of the runway de-icing products (RDPs) contain potassium formate, potassium acetate, sodium acetate, sodium formate and sometimes also glycol that may have a negative effect on aquatic life surrounding the airports.

The *bare runway* is therefore applied by airports to increase passenger and employee safety ensuring runway practicable by making winter contaminants easier to remove. Work needs to be carried out to reduce costs and environmental impacts (ground and surface water contamination), by increasing knowledge regarding de-icing and anti-icing performance of RDPs as a means of optimizing operations [14]. Knowing product performance is essential for airports to select the appropriate amount of product in relation to the conditions experienced on the ground. Therefore, laboratory tests of such products are required under known and controlled conditions [15-17]. Currently, three aerospace standards are applied to evaluate the performance of an RDP [16, 18]; the tests, undertaken jointly and in a systematic manner, are the ice melting, ice undercutting, and ice penetration tests.

The ice penetration test follows the AS6211 test method standard [16] and involves recording the vertical penetration depth of the product into the ice (mm/min). The test illustrates how a product, under ideal conditions, enters the ice by melting it down vertically. Trzaskos et al. [19] evaluated ice penetration under prewet conditions; however, they did not follow the AS6211 protocol. They used a clear ice substrate and then modeled the ice penetration of the RDP. A relatively slow ice penetration rate was easily observable by photo analysis. In this work [19] solid NaCl and liquid $MgCl_2$ in a prewet mode were used, two products which should be avoided for use on runways due to their corrosiveness on aircraft components.

The ice undercutting test is performed according to the AS6172 test method standard [17]. The test gives the area that the RDP can clear, hence a two-dimensional result (mm^2), under the ice cover, per minute. The test informs on how a product eases debonding when the RDP reaches the underside of the ice. The available literature discussing this topic is nonetheless inexistent, highlighting the need for research in this area. This test was not run in this study.

Finally, the ice melting test estimates the ice mass that an RDP will melt per minute. This test is described by the AS6170 test method standard [15]. A product that melts a greater amount of ice and a good ice penetration is deemed to be more effective. This test result is in three-dimensions (mass/volume per minute) and represents the speed at which a product melts ice. The ice melting capacity has also been evaluated using ice cubes [20] and insulated bottles [21] which are not included properly in the standard because of the variability of the parameters. In these tests, a marked lowering of the temperature occurs upon the fluid contacting the ice surface reflecting an endothermic reaction with a dilution of the brine. Another method grows the ice by very thin layers—0.5 mm layers accumulated to a final thickness of 25 mm—to limit the formation of bubbles and obtain an equal contact surface between the RDP and the ice [22] [23]. The studies that applied this method observed that the diffusion flux, dimension of which is the amount of material per unit area per unit time, correlated well with the ice melting rate. Nevertheless, in this study we follow the AS6170 test method protocol [15] as it fits closer to the reality of winter operations in Canada. Moreover, this method is preferred as it is well known, easy to conduct, and, most importantly, all involved parameters of this test are known.

The main objective of this article is to present a numerical model of the ice penetration method using laboratory-based tests of RDP ice penetration and ice melt, to validate the model output. The model will serve to develop new methods of analysis of fluid RDP behavior on ice and improve our understanding of RDP–ice interactions.

2. Experimental protocols

We performed ice penetration and ice melting tests in a controlled laboratory setting. The third test related to RDP–ice interactions, ice undercutting, was not applied. All tests were run in a controlled climatic chamber at −2 °C and −10°C. We selected potassium acetate diluted by 50% in demineralized water, in fluid form, as the RDP for both tests.

2.1. Ice penetration protocol

We followed the AS6211 test method standard [16] for the ice penetration test (Figure 1). We carried out the test in a cold room of the International Laboratory of Anti-icing Materials (AMIL). This cold room (9.1 m high, 5.5 m long, and 3.5 m wide) provides a controlled air temperature between 0 °C and −35 °C at a precision of 0.5 °C.

We obtained ice by pouring 0.5 mL of ASTM D1193 type IV water into a Pyrex test tube. The fluid and the test tube holder were placed in the chamber at least eight hours before the test to ensure they attained the required test temperature. The 6 mm × 50 mm Pyrex test tubes were then placed on the holder for 15 min. Using a syringe, we added 0.45 ± 0.05 mL of demineralized water into each tube by pushing the needle into the bottom of the tube and raising it gradually to avoid air bubble formation. We left the water 2 h for it to freeze; we used a needle (having the same temperature as the chamber) to initiate ice formation by gently touching the water surface. After

30 min, the ice interface inside the glass tubes was flattened using an aluminum bar (3.75 mm diameter and preheated with hot water between 65 and 70 °C) to obtain a smooth ice surface without asperities. Finally, the support and the glass tubes were maintained at constant temperature in the cold room at −10 ± 0.5 °C for an additional 90 min before proceeding with the tests. The chamber temperature was either maintained at −10 °C or increased to −2 °C as per the AS6211 test method.

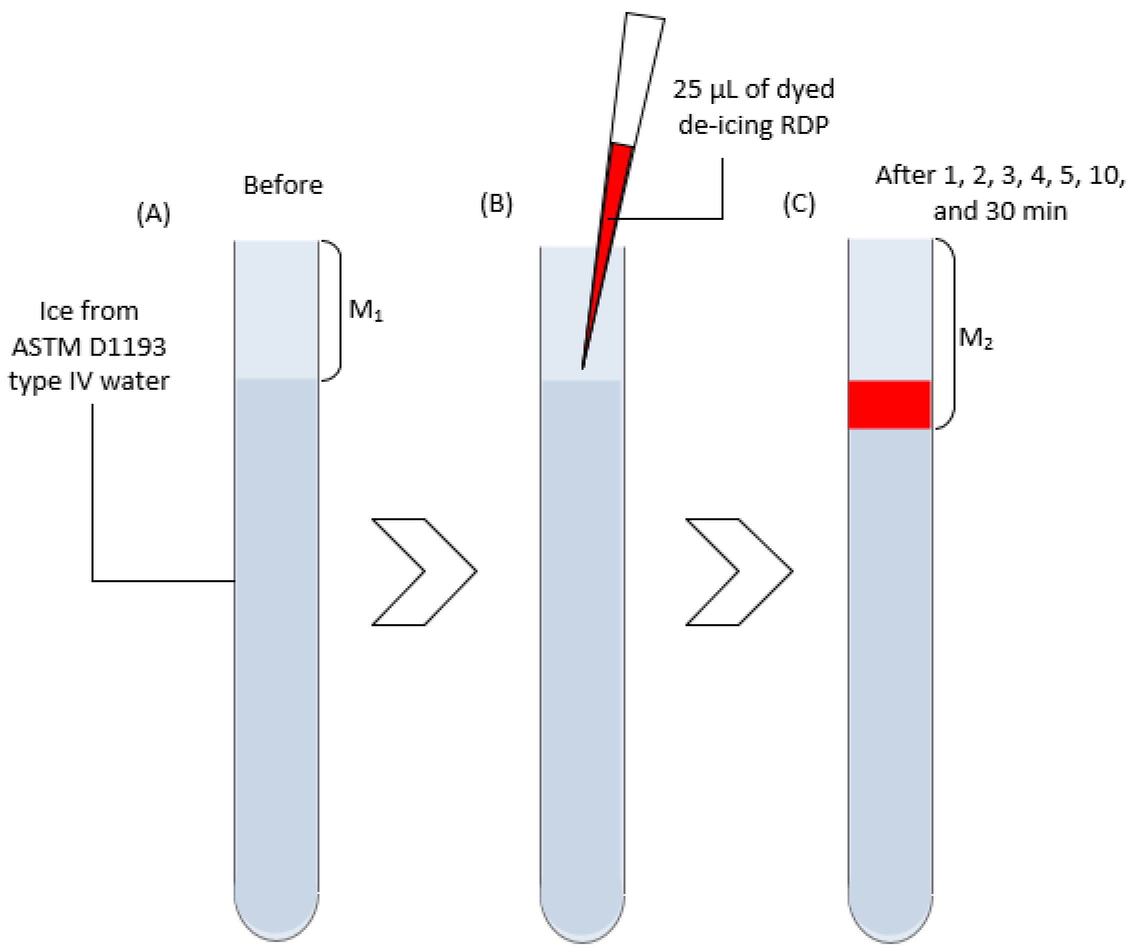

Figure 1. Ice penetration test of a runway de-icing product (RDP) according to the AS6211 standard. (A) Initial ice samples in microcentrifuge tubes; (B) deposition of the dyed RDP (potassium acetate) onto the ice sample; and (C) the RDP penetration of the ice [16]

The ice penetration test method was performed according to AS6211 standard [16]. Prior to adding the fluid, we measured the height from the top of the tube to the ice surface (measurement M_1). We then poured 25 µL of the dyed RDP into the tube. We used rhodamine B as a dye as it does not alter RDP performance [16] and helps to accurately determine RDP penetration. Measurements (M_2) were then taken after 1, 2, 3, 4, 5, 10, and 30 min, measuring from the top of the tube to the depth of fluid penetration. Ice penetration was calculated by subtracting M_1 from M_2. We used a camera to increase the precision of the measured depths and processed the photos using ImageJ software, which measures to the nearest of a pixel. The data was then converted into millimeters. We repeated the test four times [1]. There is no failure value or performance limit specified in this standard.

The ice melting test method was performed according to the AS6170 test method standard [15] (Figure 2). In a first step, we placed a Petri dish in a −10 °C cold room and filled it with 60 mL of ASTM D1193 type IV water. After a minimum of 8 h, we weighed the Petri dish and the formed ice using a calibrated two-decimal scale. We then poured 5 g of RDP onto the ice sample. We used a thermal camera— (Optris Pi400) and the associated software (Optris PIX Connect)—to this procedure to improve data collection and to better understand product performance. The thermal camera recorded thermal imagery video to determine temperatures during ice melting.

Experimental results

2.2. Ice penetration test

Photos captured during the ice penetration test highlight the general behavior of the product (Figure 2). We observed that fluid penetration into the ice was initially quite rapid (Figure 3). Ice penetration by the RDP was also greater in the −2 °C ice than for ice at −10 °C.

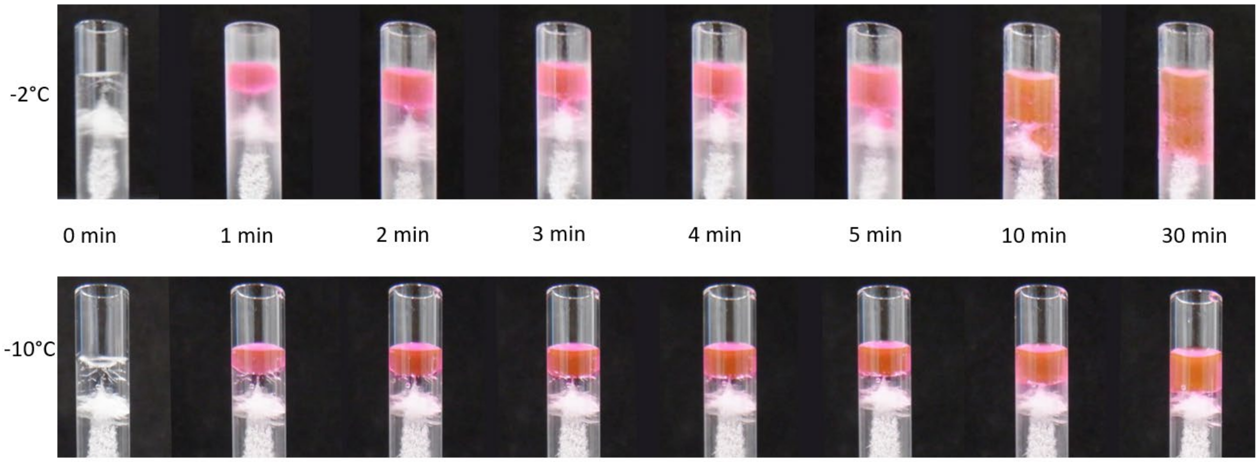

Figure 2. Evolution of fluid penetration into the ice during the ice penetration test for the RDP (potassium acetate) at −2 °C (top) and −10 °C (bottom). The color change is more evident for the samples at −2 °C, testifying to the dilution of the brine that penetrates the ice.

Moreover, fluid penetration was not uniform, showing a more pointed (inverted conical) shape, which then tends to flatten out. A similar form was observed by Trzaskos and Klein-Paste [19]. The color of the RDP is also lighter in the −2°C test, indicating that the dilution is then more important at −10°C.

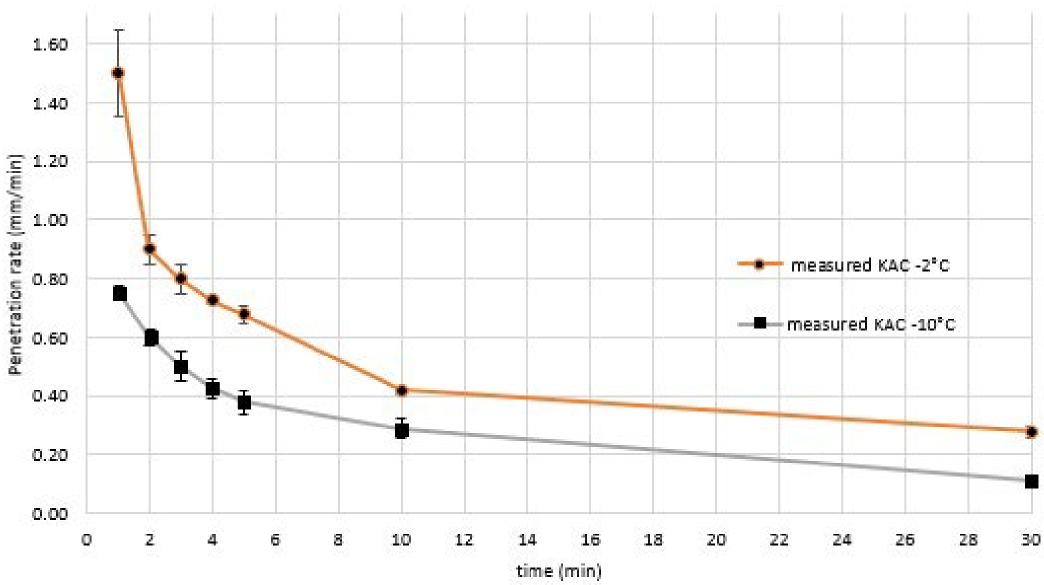

Figure 3. Ice penetration rate of the 50% w/w potassium acetate KAC at −10 °C and −2 °C

In regard to the penetration rates of the RDP at −2°C and −10°C, the product was most effective in the first minutes; for both ice temperatures, the penetration rates decreased over the next 30 min along an inverse logarithmic curve (Figure 3). However, the ice penetration rate at −2 °C was greater than that for the −10 °C ice; nonetheless, the standard deviation was greater for −2 °C than −10 °C after one minute (±0.3 at −2°C and ±0.05 at −10°C). As a second step, we analyzed the thermal video to gain insight into RDP behavior in the Petri dish (Figure 4).

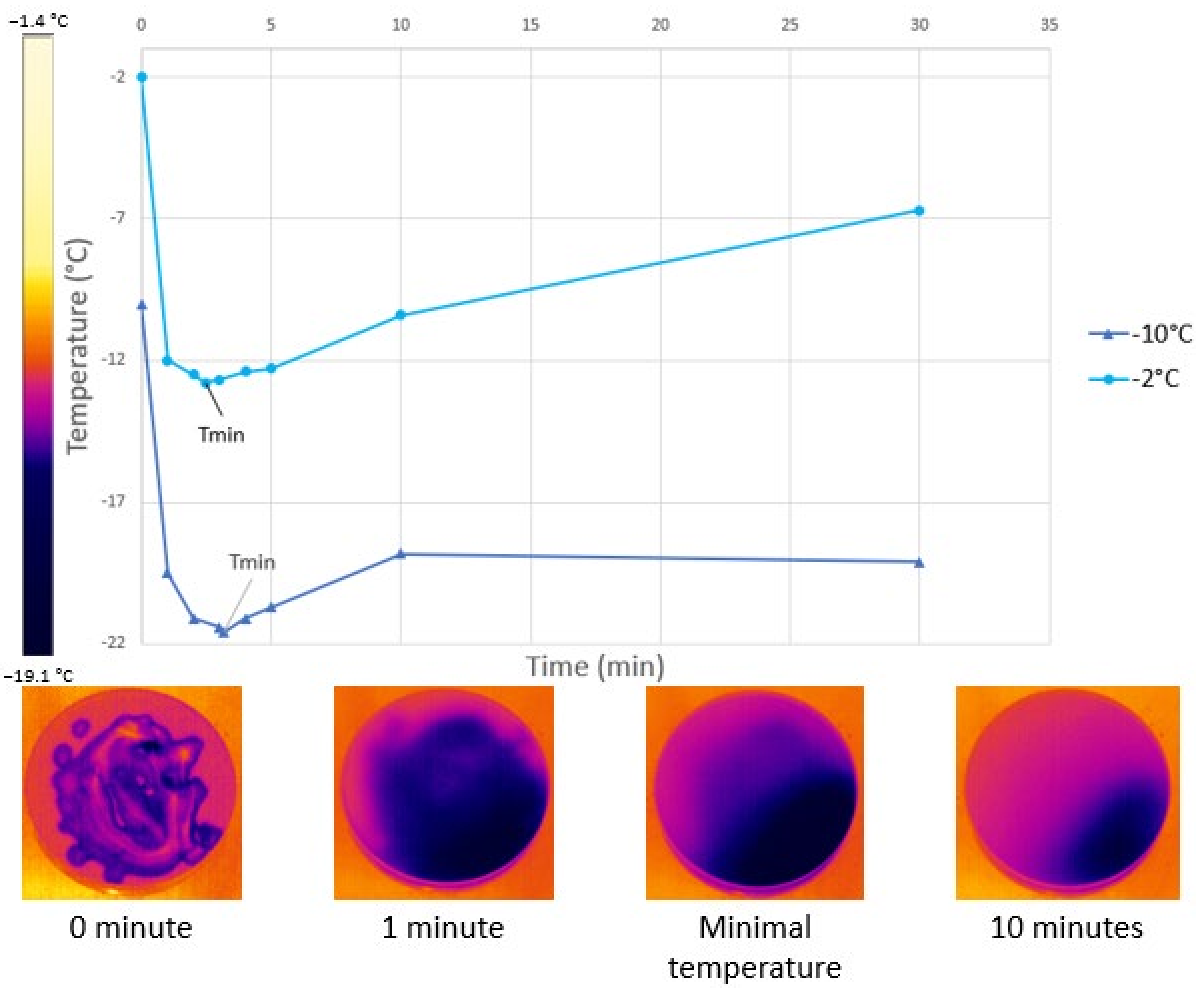

Figure 4. Minimum temperatures of the RDP (potassium acetate) at the ice surface for −10 °C and −2 °C and the thermal photographs at the ice surface at −10 °C during the ice melting test at 0, 1, minimal temperature, and 10 min.

Temperature was not uniform across the surfaces, varying from −10 °C to minimum values around −20 °C (Figure 4). At T_0, we observed an instantaneous temperature drop at the beginning of the test. The reaction is endothermic because of the dissolution of salt in water/ ice [22]. A minimum temperature of −21.6 °C, corresponding to the product's peak effectiveness, therefore where the product is the most reactive, was attained after three minutes, and the temperature then increased until the final observation at 30 min. The minimum temperature reached at −10 °C was −21.6 °C at 189 s and −12.8 °C at 148 s for the −2 °C tests. The temperature eventually attained the test temperature, −10 °C, when the product could no longer melt the ice. The pattern of minimum temperatures over the course of the melting capacity test [15] at −2 °C and −10 °C is important for modelling how the product penetrate the ice .

The attained minimum temperature was lower at −10 °C than at −2 °C, which is understandable. Nevertheless, the difference between the initial temperature of the test and the minimum temperature reached was 10.8 °C for −2 °C and 11.6 °C for −10 °C. This pattern of delta temperatures is explained by ice melting with aqueous solutions below 0 °C being limited by diffusion [23]. The temperature of the product drops following the same trend. The higher the melt rate, the lower the temperature. We can therefore conclude that the greater the penetration rate, the lower the temperature from the correlation between both methods.

3. Ice penetration modeling

3.1. Simplified mathematical modeling of ice penetration

We used our observations to develop a simplified thermodynamic model presenting the evolution of ice penetration in the presence of a RDP following the AS6211 protocol [16]. As a first step, we evaluated the thermodynamic evolution of the ice penetration test to determine whether it acts as the natural convection of a liquid in a cavity in the presence of a phase change. It is crucial to determine the type of convection since it will drive the selection of the accurate equations. Forced convection will rather complexify the model equations. The immediate melting of a solid, such as ice crystals, occurs upon contact with the RDP because of the lower melting point for the water molecules (and RDP) at the contact with the ice.

To determine whether this assumption of natural convection of the RDP is applicable to our tests, we relied on a series of visual recordings, using a digital lens at 12× magnification, to observe whether RDP circulated when deposited onto the ice sheet in an initially isothermal condition. Heitz et al. [24] identified three possibilities or modes of heat transfer in water contained within a closed cavity: conduction, laminar or turbulent convection; their respective occurrence mainly depends on the temperature profile, the velocity profile, and the dimensions of the cavity (L/D; height/width). The authors identify the critical Rayleigh number (Ra_c) and the geometrical parameters of the cavity as predictors of heat transfer mode in the cavity.

Our recordings portray a bottom–top circulation of the fluid and a well-defined circulation cell, as described in the literature [24]. The RDP flow profile shows flow channels from bottom to top and then top to bottom (Figure 5). Measurements of the fluid surface temperature using a thermal camera recorded a considerable drop in the fluid surface temperature after the start of the test (up to 10 °C cooler), which suggests the mode of heat transfer by natural convection is similar to that for a cavity having the bottom (ice) at a higher temperature than the top (fluid).

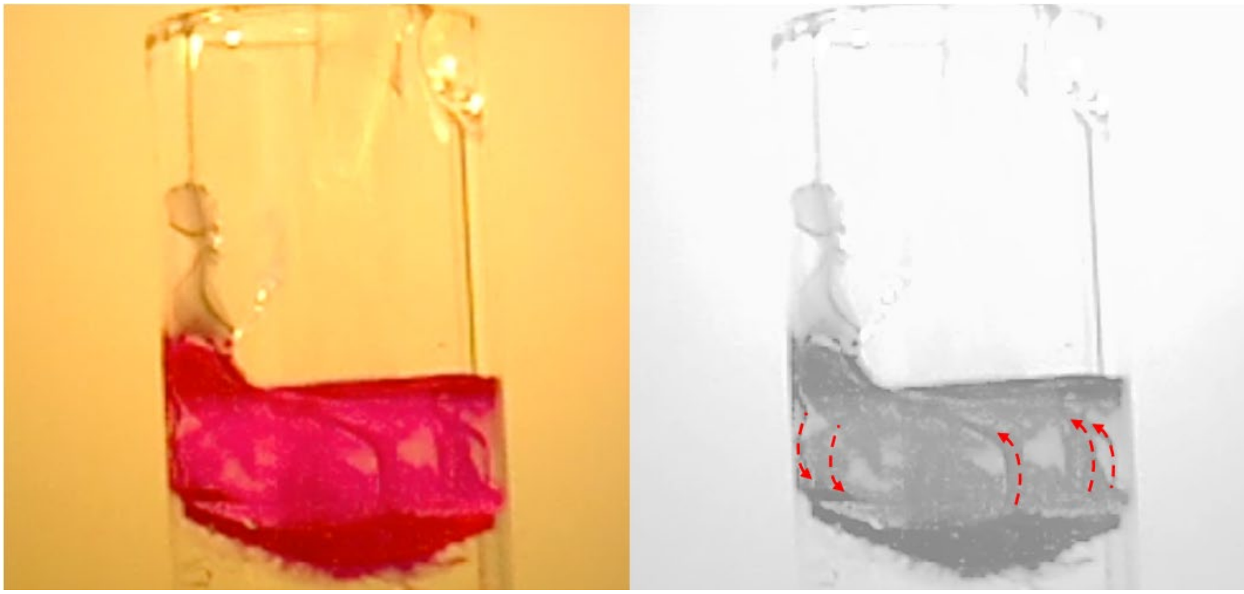

Figure 5. Visual evidence of natural convection by a bottom–top circulation followed by top–bottom circulation of the RDP when applied to the ice layer. Image on the right has red arrows added to show this convection

Our measurements of the surface temperature of the RDP and our recorded observation confirm that it circulated following a natural convection model (Figure 5). We can validate this observation by comparing the measured penetration rates with the model output and by estimating the critical Rayleigh number for predicting the mode of heat transfer. The important parameters to consider in the case of this cavity are as below:

- the dimension of the cavity and in particular the ratio height/width (L/D),
- the properties of the RDP at the test temperature T, such as concentration, viscosity.
- the properties of the ice at the test temperature T,
- the Rayleigh (Ra), Nusselt (Nu), Prandtl (Pr), and Grashoff (Gr) numbers
- the modes of heat transfer (bottom–top or top–bottom),
- the presence of a phase change of the ice (melting/fusion).

3.1.1. Energy balance around the cavity

Rigorous modeling of phenomena involving a phase change frequently uses the enthalpic method [25], which makes it easier to consider the constant temperature plateau at the melting temperature. Fluid enthalpy evolves constantly during the melting temperature plateau via the storage of internal energy until the melting point; this results in a continuous energy function. However, we wish to apply a simplified approach to observe in a general way the ice melting phenomenon and to draw some useful conclusions. We can refer to Figure 6 to illustrate the main assumptions of this modeling approach. The main assumptions of the simplified model are that:

- at $t = 0$, the RDP, the ice, the tube, and the outside air all have the same temperature T as the climatic chamber T_0 (isothermal).
- the temperatures of the fluid T_2, melted ice T_3, and ice T_1 are lumped parameters; heat transfer is considered dominant in the axial direction of the tube (1D lumped parameter model),
- the temperature of the sample tube T_4 is the same temperature as that of the climate chamber T_0,
- the concentrations of potassium acetate in the C_2 and C_3 fluid are grouped parameters,
- the phase change of the ice and melting rate is a function of the temperature difference between the temperature of the fluid T_2 and the melting temperature of the fluid at concentration C_2, i.e., $T_2 - T_{di}$.
- In this first version of this model, the thermodynamic properties (ρ, Cp, k, v) of brine and RDP are assumed to be the same as the water. However, in a future version, different properties between brine and water could be added [26].

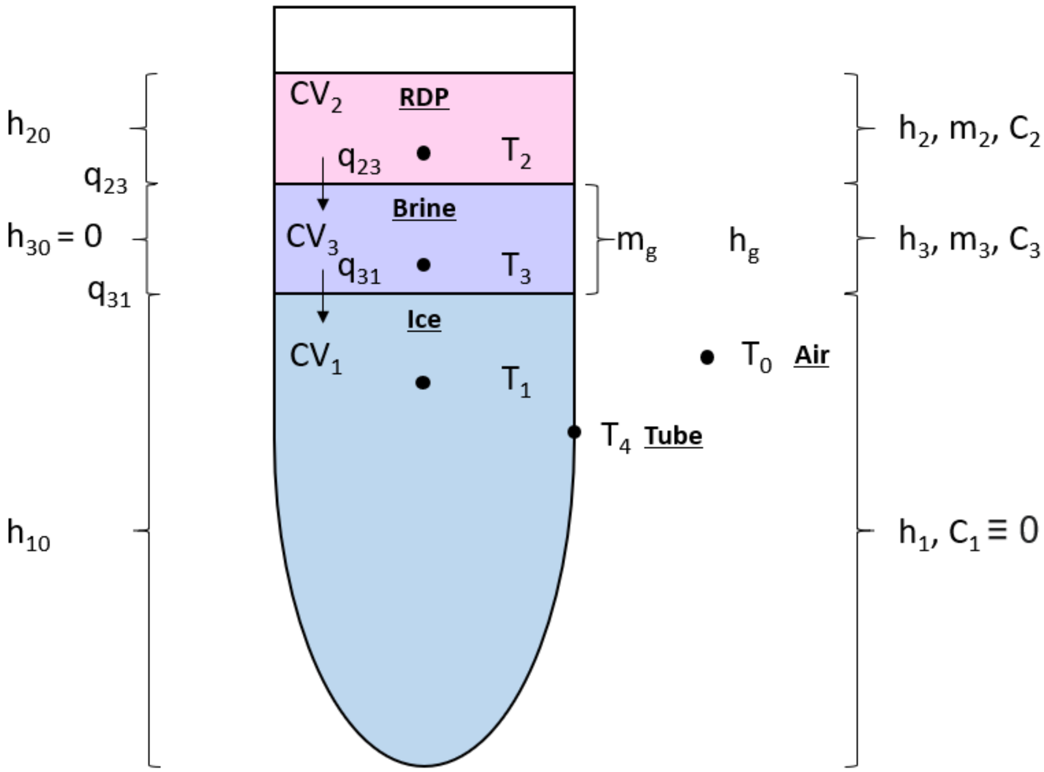

Figure 6. Representation of the elements of the 1D thermodynamic model of the ice penetration test following the AS6211 test method protocol [16]

The resulting model has a natural convection cell of the RDP in the lower part, near the ice interface, when the RDP is deposited onto the ice, the temperature of the lower part decreases to a temperature cooler than that of the ice because of heat transfer to the melting ice (latent heat of fusion of the ice H_{sl}). This convection cell occurs when a positive thermal gradient $\nabla T = T_1 - T_3$ becomes established. Heitz presents the critical Rayleigh number Ra_c for the heat transfer modes in water contained within a cavity of dimension L/D. For the test tube filled with RDP, we obtain a ratio of 3.6 mm/4 mm = 0.9. The *R*a around the RDP above the ice layer is expressed as a function of the RDP thickness, which increases as the ice is penetrated, and thus melts.

$$Ra = \frac{g\beta_2}{\nu\alpha}(T_1 - T_3)(x_2 + x_3)^3 \,. \qquad (1)$$

We observe that in the case of a typical simulation of the test tube (L/D = 0.9), conduction is the dominant mode over the first minutes (Figure 7). This mode then evolves toward a natural convection until the end of the test (30 min). Thus, we observe that the dominant mode of heat transfer is laminar natural convection.

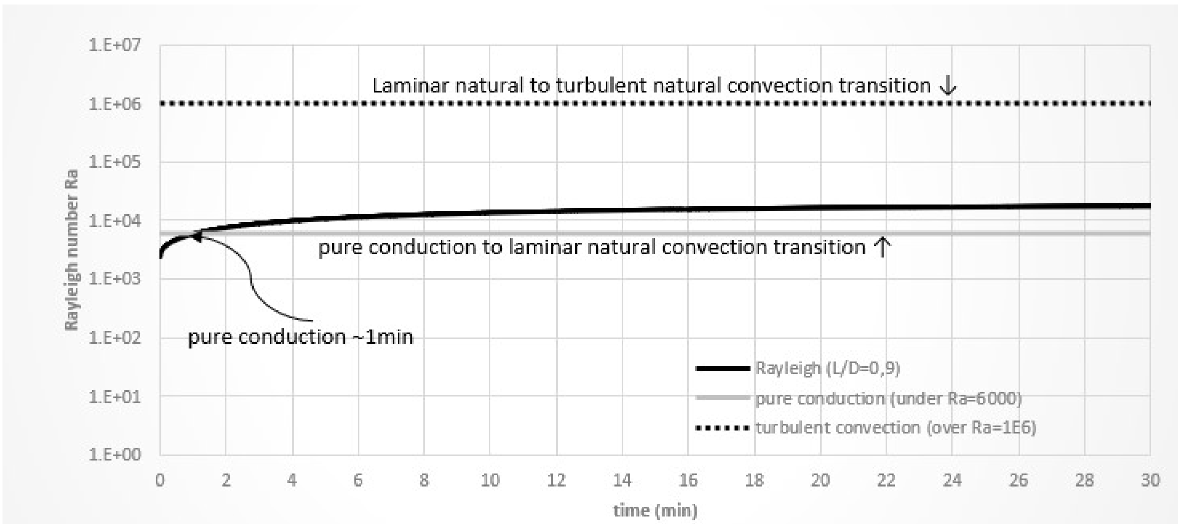

Figure 7 : Rayleigh number in the test tube cavity (L/D = 0.9) and heat transfer mode

The heat and mass balance equations of the different control volumes are

CV1 (ice):

$$\dot{E}_{CV1} \sim m_1 C_{p1} \dot{T}_1 = \rho_1 A_1 x_1 C_{p1} \dot{T}_1 = q_{31} + q_{41} \,, \qquad (2)$$

$$\dot{m}_1 = \rho_1 A_1 \dot{x}_1 = -\dot{m}_i \,; \qquad (3)$$

CV2 (RDP):

$$\dot{E}_{CV2} \sim m_2 C_{p2} \dot{T}_2 = \rho_2 A_2 x_2 C_{p2} \dot{T}_2 = -q_{23} + q_{42} + q_{02} \,, \ (4)$$

$$\dot{m}_2 = 0 \quad (5) \,;$$

CV3 (brine):

$$\dot{E}_{CV3} \sim m_3 C_{p3} \dot{T}_3 = \rho_3 A_3 x_3 C_{p3} \dot{T}_3 = q_{23} - q_{31} + q_{43} - \dot{m}_i H_{sl} \,, \ (6)$$

$$\dot{m}_3 = \rho_3 A_3 \dot{x}_3 = \dot{m}_i \,, \qquad (7)$$

$$C_2 = C_3 = \frac{m_i}{m_{tot}} = \frac{C_2(0) m_2(0)}{m_2(0) + m_3} \ \ (\mathrm{CV}_2 \text{ and } \mathrm{CV}_3) \,; \qquad (8)$$

and the thermal flows:

$$q_{31} = h_{31}A_{31}(T_3 - T_1)\,, \qquad \textit{(9)} \text{ (brine to ice)}$$

$$q_{41} = \frac{2\pi k_4 x_1}{ln(^{r_0}/_{r_i})}(T_4 - T_1)\,, \qquad \textit{(10)} \text{ (tube to ice)}$$

$$q_{23} = h_{23}A_{23}(T_2 - T_3)\,, \qquad \textit{(11)} \text{ (RDP to brine)}$$

$$q_{42} = h_{42}A_{42}(T_4 - T_2)\,, \qquad \textit{(12)} \text{ (tube to RDP)}$$

$$q_{02} = h_{02}A_{02}(T_0 - T_2)\,, \qquad \textit{(13)} \text{ (air to RDP)}$$

$$q_{43} = h_{43}A_{43}(T_4 - T_3)\,; \qquad \textit{(14)} \text{ (tube to brine)}$$

the interchange areas:

$$A_{31} = A_{23} = A_{02} = \pi r^2\,, \qquad \textit{(15)}$$

$$A_{41} = 2\pi r x_1\,, \qquad \textit{(16)}$$

$$A_{42} = 2\pi r x_2\,, \qquad \textit{(17)}$$

$$A_{43} = 2\pi r x_3\,; \qquad \textit{(18)}$$

the exchange coefficients:

$$h_{02} = 0.64(\Delta T/L)^{1/4} = 0.64\big((T_0 - T_2)/x_2\big)^{1/4}\,, \qquad \textit{(19)} \text{ (air to liquid) [27]}$$

$$h_{42} = h_{43} = 1.42(\Delta T/L)^{1/4} = 1{,}42\big(T_4 - T_{2/3}\big)^{1/4}\,, \qquad \textit{(20)} \text{ (tube to liquid, laminar) [28]}$$

$$h_{31} = \frac{0.13\,k_3}{x_3}\Big(R_{a_{x_3}}\Big)^{0.2}\,, \textit{(21)} \text{ (brine to ice, laminar) [29]}$$

$$h_{23} = \frac{0.13\,k_2}{x_2}\Big(R_{a_{x_2}}\Big)^{0.2}\,, \qquad \textit{(22)} \text{ (RDP to Brine, laminar) [29]}$$

$$\dot{m}_i = \dot{m}_0\left[\frac{T_3(t) - T_{di}(t, C_2(t))}{T_3(0) - T_{di}(0, C_2(0))}\right]^2\,; \quad \textit{(23)}$$

and the following values of the parameters: The values of ρ_1, k_1, C_{p1} are the usual properties of water and ice.

$$R_{a_{x_3}} = \frac{g\beta_3}{\nu_3\alpha_3}(T_1 - T_3)x_3^3 \;, \qquad (24)$$

$$R_{a_{x_2}} = \frac{g\beta_2}{\nu_2\alpha_2}(T_2 - T_3)x_2^3 \;, \qquad (25)$$

$$r = 2\ x\ 10^{-3}[m]\ \ (test\ tube\ radius)\;, \qquad (26)$$

$$k_1 \sim 2.1\ \left[\frac{W}{mC}\right]\ \ (0\ to - 20[°C])\;, \qquad (27)$$

$$C_{p1} \sim 2040\ \left[\frac{J}{kgC}\right]\ \ (0\ to - 20[°C])\;, \qquad (28)$$

$$\rho_1 \sim 920\ \left[\frac{kg}{m^3}\right]\ \ (0\ to - 20[°C])\;, \qquad (29)$$

$$C_{p2} = C_{p3} \sim 2400\ \left[\frac{J}{kgC}\right]\ \ (0\ to - 20[°C])\;, \qquad (30)$$

$$\rho_2 = \rho_3 \sim 1000\ \left[\frac{kg}{m^3}\right]\ \ (0\ to - 20[°C])\;, \qquad (31)$$

$$k_2 = k_3 \sim 0.555\ \left[\frac{W}{mC}\right]\ \ (0\ [°C])\;, \qquad (32)$$

$$H_{sl} = 3.33\ x\ 10^5\ \left[\frac{J}{kg}\right](enthalpy\ of\ ice\ fusion)\;, \qquad (33)$$

$$C_2(0) = 0.5\left[\frac{kg\ of\ deicing\ fluid}{kg\ total}\right], \qquad (34)$$

$$T_{di}(t, C_2) = -134.2C_2(t)^2 - 42.1C_2(t)\;, \qquad (35)$$ (KAC, see Figure 8)

This equation is based on the polynomial second order fitting of the phase diagram of KAC and water (Figure 8).

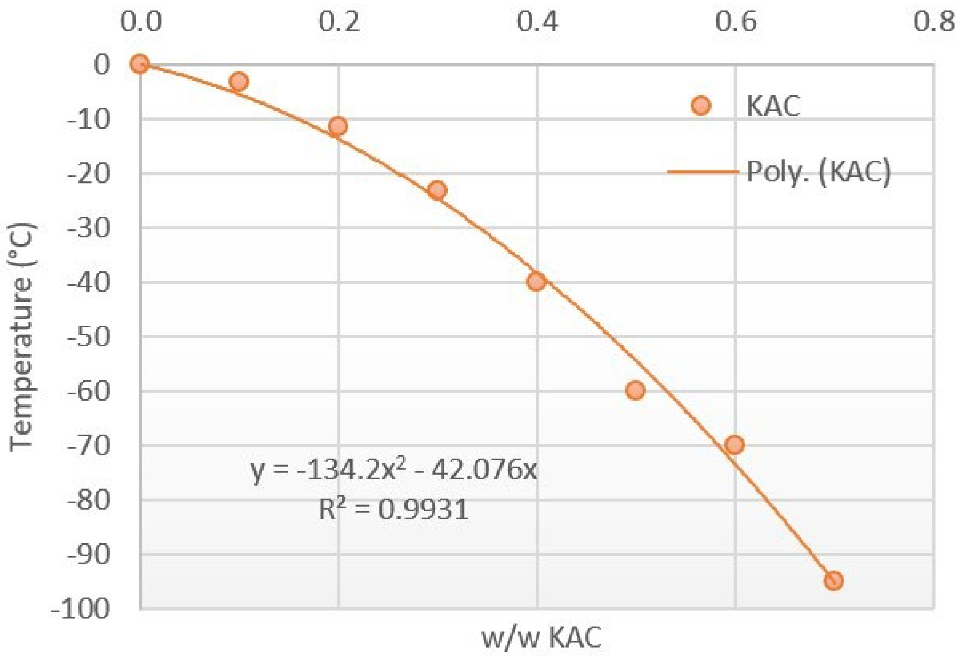

Figure 8 : Theorical freezing temperature of KAC in water. Polynomial second order fitting is obtained from those data.

The following values are the calibration values at t=0 (Figure 3).

$$\dot{m}_0 = 1\ to\ 3\ x\ 10^{-7}\left[\frac{kg}{s}\right]\ \ (ice\ melting\ rate\ at\ t = 0)\ , \qquad (36)$$

$$\beta_2 = \beta_3 \sim 2.1\ x\ 10^{-4}[C^{-1}]\ \ (liquid\ thermal\ expansion\ at\ T = 0°C)\ , \ (37)$$

$$\upsilon_2 = \upsilon_3 \sim 1.8\ x\ 10^{-6}\left[\frac{m^2}{s}\right]\ \ (liquid\ kinematic\ viscosity\ at\ T = 0°C)\ , \ (38)$$

$$\alpha_2 = \alpha_3 \sim 1.4\ x\ 10^{-7}\left[\frac{m^2}{s}\right]\ \ (liquid\ thermal\ diffusivity\ at\ T = 0°C)\ . \qquad (39)$$

3.2. Solving the nonlinear differential equations

The analytical solution for the five differential equations $(T_1, T_2, T_3, x_1, x_3)$ is complex; thus, we applied a first-order finite difference numerical method. From experimental measurement, we obtain:

$$(T_1(0) = T_2(0) = T_3(0) = -2\,, -10, x_3(0) = 0, x_1(0) = 0.04, x_2(0) = 0.0036, C_2(0) = 0.5)$$

For the simulated ice melt rate profiles, we observed a good match with the experimental results obtained at −2 °C and −10 °C. The model's initial penetration rates were lower than the observed rates; this discrepancy can be explained mainly by variability between measurements of ice penetration depth recorded in the center of the tube. Measurements in the center of the tube partly overestimate ice penetration along the sides (concave meniscus) because the model predicts a uniform penetration depth for the entire section.

In the model, the fluid cooled considerably when melting began; however, the temperature remained above the melting temperature of the RDP (Figure 9). The observed temperature difference between the RDP and the melting point (Figure 10) indicates well the performance of the RDP because ice melting continues as long as the temperature of the RDP remains above the melting temperature at concentration C (Figure 11). We also noted the constant dilution of the de-icing fluid over time (Figure 12).

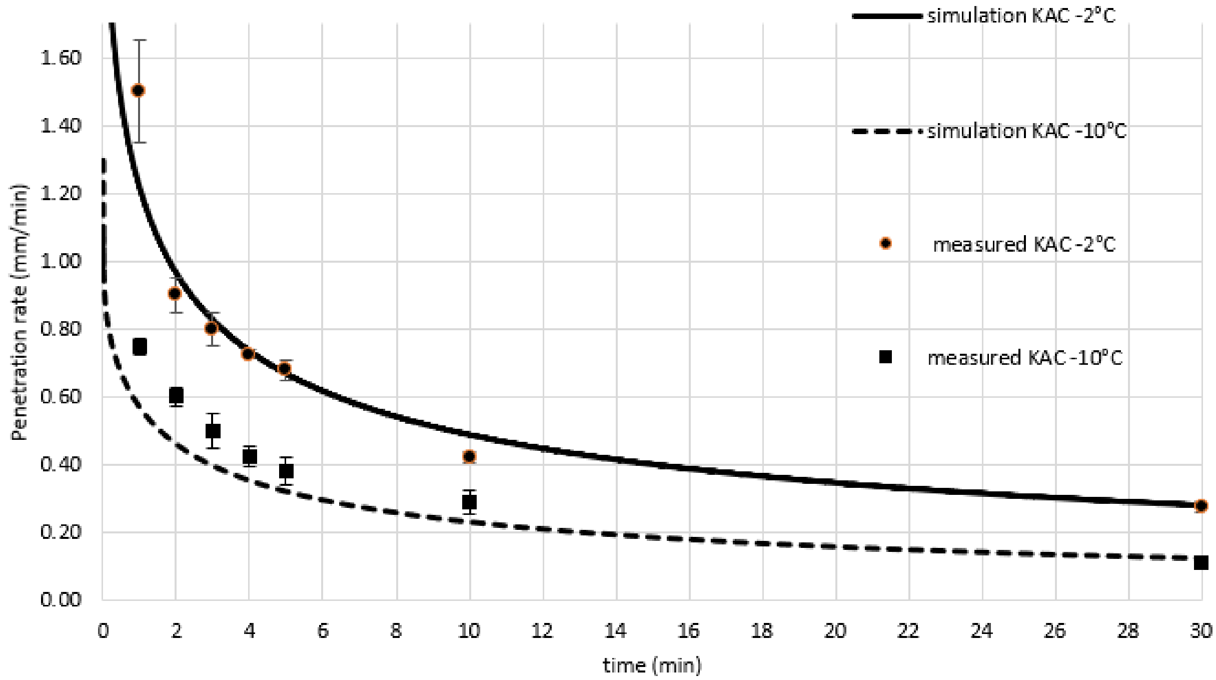

Figure 9. Simulated ice penetration rate profiles for −2 °C and −10 °C for KAC as an RDP

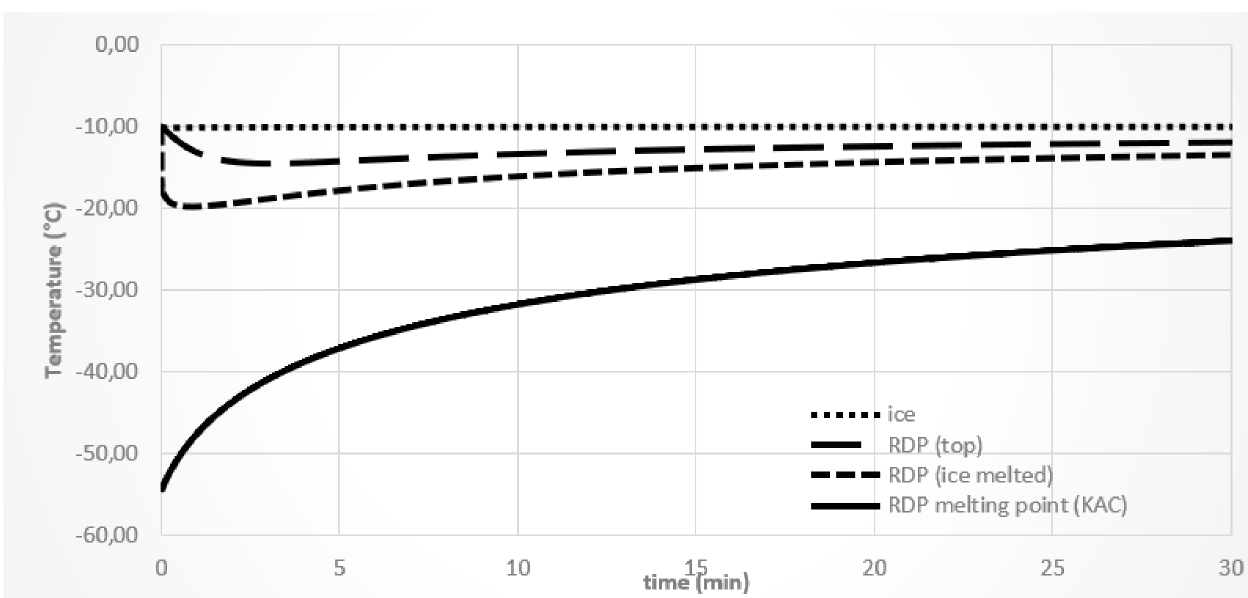

Figure 10. Simulated temperature profiles for the −10 °C test

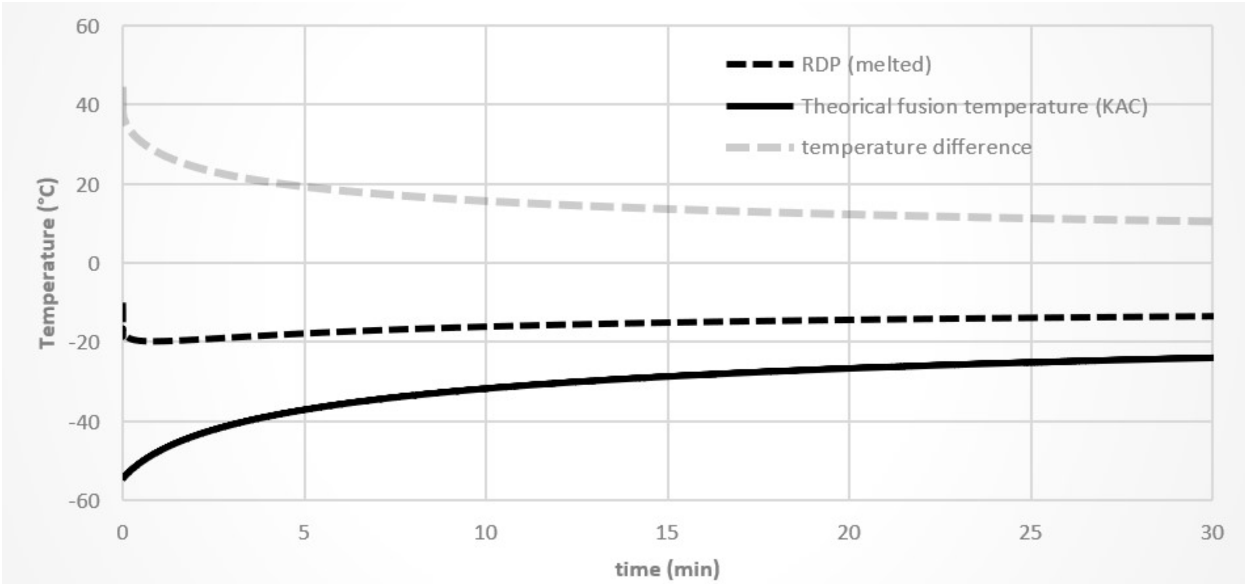

Figure 11. Temperature difference between the de-icing fluid T_2 and the melting value T_{di} for the test at -10°C

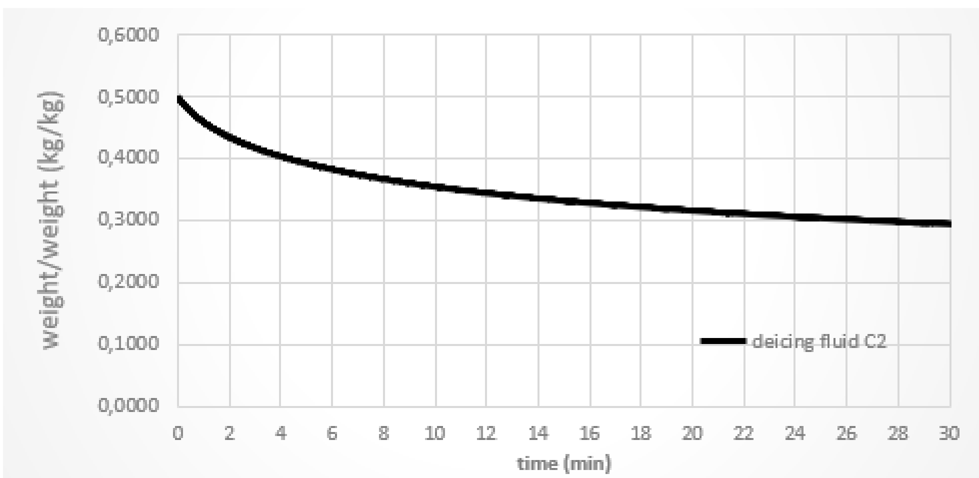

Figure 12. C_2 concentration of de-icing fluid over time for the −10 °C test

3.3. Verification of the numerical solution (energy balance and steady-state solution)

To verify the obtained numerical solution, we used the energy balance equation of the simulation to determine the convergence of the solution and the isotherm at which the de-icing fluid becomes diluted and the melting ends.

We can write the energy balance equation for the entire tube (CV_1, CV_2, and CV_3) as

$$E_{in} - E_{out} = \Delta E_{tot} \, , \qquad (40)$$

$$\int_0^{30\,min} \sum_1^4 q_i \, dt - 0 = \sum_{i=1}^{3} E_{CVi} + \Delta E_{ice\ melted} \, , \qquad (41)$$

$$\int_0^{30\,min} [q_{02} + q_{41} + q_{42} + q_{43}] \, dt = m_3 H_{sl} + \Delta E_{CV1} + \Delta E_{CV2} + \Delta E_{CV3} \, . \qquad (42)$$

Expressed in terms of a percentage error, we find

$$\%\, energy\ balance = 100 \left(\frac{E_{in} - \Delta E_{tot}}{E_{in}} \right), \qquad (43)$$

$$\%\, energy\ balance = 100 \left(\frac{\int_0^{30\,min} [q_{02} + q_{41} + q_{42} + q_{43}] dt - m_3 H_{sl} - \Delta E_{CV1} - \Delta E_{CV2} - \Delta E_{CV3}}{\int_0^{30\,min} [q_{02} + q_{41} + q_{42} + q_{43}] dt} \right). \qquad (44)$$

We calculate the values for the energy balance of the simulation at −10 °C,

$$\%\, energy\ balance = 100 \left(\frac{16.55J - 15.93J}{16.55J} \right) = 3.7\% \, . \qquad (45)$$

As the solution temperature approaches the isotherm, ice penetration continues until the maximum de-icing power of the RDP is reached. When we assess the obtained temperatures during the 780 min of melting, we note that all temperatures converge to the temperature of the climate chamber at −10 °C. At −10°C, the obtained RDP concentration reaches 0.16, which is the minimum concentration reached when the ice melt ends at −10 °C. The model appears valid for calculating energy balance. The time to reach thermal equilibrium is long because the heat exchange coefficients *h* is a function of the temperature difference, which proportionally lengthens the time to reach thermal equilibrium.

3.4. Maximum de-icing power of a fluid

From the model and the experimental results [16], we can determine that the maximum de-icing power of a surface A covered with ice, of a fluid at a temperature T, starting concentration C_2, and starting thickness x_2 corresponds to the complete melting of this layer of ice of thickness x_1 until reaching the minimum concentration C_{min} of the melting curve of the fluid at this temperature . The equation that governs this maximum de-icing power is:

$$C_{min} = \frac{C_2 \rho_2 A x_2}{\rho_2 A x_2 + \rho_1 A x_1} = \frac{C_2 \rho_2 x_2}{\rho_2 x_2 + \rho_1 x_1}. \qquad (46)$$

Expressed in terms of the layer of RDP required to achieve complete melting of the ice, we can write

$$x_2 = \frac{\rho_1}{\rho_2} \frac{C_{min}}{(C_2 - C_{min})} x_1 \sim 0{,}92 \frac{C_{min}}{(C_2 - C_{min})} x_1 . \qquad (47)$$

We can express Equation 47 for a temperature T and the expression of the melting curve of the RDP (square root of Equation $T_{di}(t, C_2) = -134.2C_2(t)^2 - 42.1C_2(t)$, *(35)*).

For potassium acetate, we obtain

$$C_{min} = 3.72\ x\ 10^{-3}\sqrt{-537\,T + 1772} - 0.156 . \qquad (48)$$

Substituting x_2 into the equation, we obtain Equation 49 to determine the amount of RDP (in this case, potassium acetate) required to ensure the complete penetration of the ice layer.

$$x_2(T, x_1.C_2) = \left(\frac{3.42\ x\ 10^{-3}\sqrt{-537\,T + 1772} - 0.143}{C_2 - 3.72\ x\ 10^{-3}\sqrt{-537\,T + 1772} + 0.156}\right) x_1 . \qquad (49)$$

For example, the required thickness (x_2) of the RDP (at 0.4 by weight, C_2) to fully melt a 10 mm layer of ice (x_1) covering a surface A at a temperature of -10 °C (T) can be calculated as

$$x_2(T, x_1. C_2) = \left(\frac{3.42\ x\ 10^{-3}\sqrt{5370+1772}-0.143}{0{,}4-3.72\ x\ 10^{-3}\sqrt{5370+1772}+0.156}\right)0.01 \sim 6\ mm\ . \qquad (50)$$

Figure 13 illustrates the equation in the form of a chart for potassium acetate. The red star represents the above case. On this graph, we illustrate four different temperature that could be encountered. The form of this graph could be interesting, after experimental validation, for a practical use of RDP application rates on a frozen surface according to this standard. As an example, using this chart, if the temperature is -5°C, with an RDP of concentration of 0.5 (w/w), if the thickness of the ice is 5 mm, we should at least put 1.5 mm of de-icing fluid to ensure a complete penetration of the ice.

Such a figure could be obtained for each commercial RDP and assist the airport maintenance operation teams to accurately select the quantity of RDP to ensure a complete and efficient de-icing. Further study is necessary to adapt this model to solid RDP and prewetted RDP. Finally, it could be applied to increase the knowledge in the anti-icing properties of RDP.

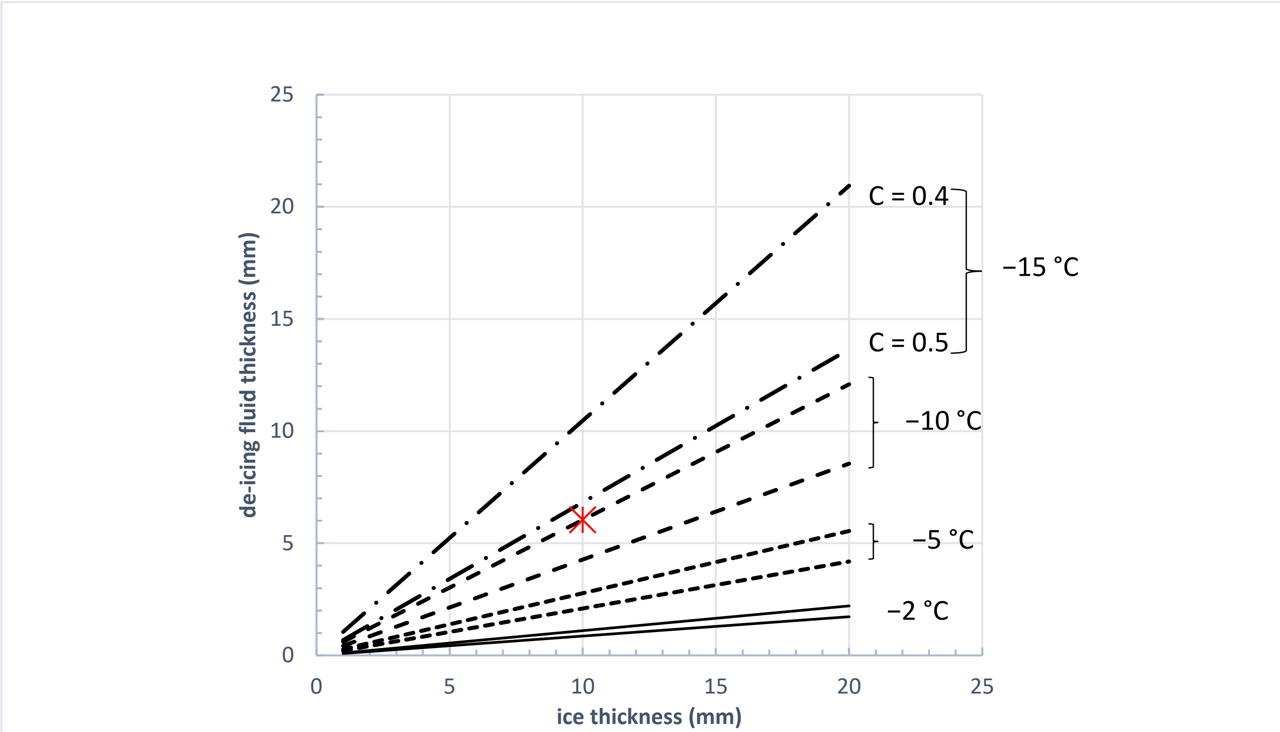

Figure 13. Thickness of the RDP as a function of ice cover thickness, temperature, and fluid concentration (C). For each temperature, the top line corresponds to a concentration (w/w) of 0.4 while the bottom corresponds to a 0.5 (w/w).

4. Conclusion

We have demonstrated that simplified ice penetration modeling, based on the AS6211 protocol [16], can reliably predict ice melt rate. Our experimental results for the ice penetration and ice melting tests confirm the model output estimates. However, one of the difficulties encountered was air bubbles, as this can affect results. In Figure 2, we can observe some air bubbles. These come from dissolved gasses in the water which are difficult to prevent.

We then obtained an equation to predict the amount of RDP required to melt a given ice thickness. The predicted penetration rates at the beginning of the test appear to be lower than the observations; however, the depth of melt at the beginning of the test is not necessarily representative of the ice melt rate of melt within the entire tube section. Fluid properties, such as the melting curve as a function of concentration, are the main factor affecting the efficiency of the products excluding, of course, the application methods in real cases. For the model, the heat transfer of the fluid when it contacts the ice is assumed to be uniform; however, in reality this is not necessarily the case. Other methods for characterizing RDP are available, and the application of our simplified model to these alternate methods could isolate the effects of diluted or undiluted solid runway de-icing products on ice melting rates.

Acknowledgement

We acknowledge the support of the Natural Sciences and Engineering Research Council of Canada (NSERC) and the Anti-icing Materials International Laboratory (AMIL). This research was conducted in support of the Consortium for Research and Innovation in Aerospace in Québec (CRIAQ) and the Ministère de l'Économie et de l'Innovation du Québec, and the support provided by Aéroports de Montréal, WPred and Nachur Alpine Solutions.

References

[1] J.-D. Brassard, C. Laforte, M. M. Tremblay, and C. Volat, "Runway Deicing Product Anti/Deicing Performance Assessment: Review and Future Directions," 2019. [Online]. Available: https://doi.org/10.4271/2019-01-1974.

[2] A. Klein-Paste, "Runway Operability under Cold Weather Conditions. Tire-pavement friction creation by sand particles on iced pavements, and non-contacting detection of sand particles on pavements," *NTNU,* 2007.

[3] A. Klein-Paste, "Airplane braking friction on dry snow, wet snow or slush contaminated runways," *Cold Regions Science and Technology,* 2017/02/20/ 2017, doi: https://doi.org/10.1016/j.coldregions.2017.02.004.

[4] A. Tuncal, U. Suat, and E. Dursun, "A MILESTONE TO ENHANCE RUNWAY SAFETY: THE NEW GLOBAL REPORTING FORMAT," *Revista de Investigaciones Universidad del Quindío,* vol. 33, no. 1, pp. 168-178, 2021.

[5] Boeing. "Statistical Summary of Commercial Jet Airplane Accidents." https://www.boeing.com/resources/boeingdotcom/company/about_bca/pdf/statsum.pdf (accessed 2022-01-19, 2022).

[6] R. Canada, "Un avion fait une sortie de piste à l'aéroport de Bagotville," 2019. [Online]. Available: https://ici.radio-canada.ca/nouvelle/1151839/incident-voyageurs-bagotville-aeroport-urgence.

[7] EASA, "Annual Safety Review," 2020. [Online]. Available: https://www.easa.europa.eu/document-library/general-publications/annual-safety-review-2020

[8] L. KORNSTAEdT and R. Lignee, "Operational Landing Distances, A new standard for in-flight landing distance assessment," *Safety,* no. 1/5, 2010.

[9] T. S. B. o. Canada. "Runway overruns." https://www.tsb.gc.ca/eng/surveillance-watchlist/aviation/2022/air-02.html (accessed.

[10] J. Procházka and M. Kameník, "Contaminated Runway Operations-Adverse weather," *MAD-Magazine of Aviation Development,* vol. 1, no. 4, pp. 3-7, 2013.

[11] Y. Niu *et al.*, "Techniques and Methods for Runway Friction Measurement: A Review of State-of-the-Art," *IEEE Transactions on Instrumentation and Measurement,* 2021.

[12] G. Comfort, "Wet Runway Friction: Literature and Information Review," 2001.

[13] J. D. Brassard, C. Laforte, F. Guerin, and C. Blackburn. *Icephobicity: Definition and measurement regarding atmospheric icing, Advances in Polymer Science*, vol. 284, pp. 123-143, 2019.

[14] (2021). *Advisory Circular (AC) No. 300-019: Global Reporting Format (GRF) for Runway Surface Conditions*.

[15] *AS6170 Ice Melting Test Method for AMS1431 and AMS1435 Runway Deicing/Anti-icing Products*, Aerospace Standard AS6170, SAE International, 2021.

[16] *AS6211 Ice Penetration Test Method for AMS1431 and AMS1435 Runway Deicing/Anti-icing Products*, Aerospace Standard AS6211, SAE International, 2021.

[17] *AS6172 Ice Undercutting Test Method for AMS1431 and AMS1435 Runway Deicing/Anti-icing Products*, Aerospace Standard AS6172, SAE International, 2021.

[18] *AMS1431D Compound, Solid Runway and Taxiway Deicing/Anti-icing*, Aerospace Material Specification AMS 1431, revision D, SAE International, June 2012 2012. [Online]. Available: http://www.sae.org

[19] M. P. Trzaskos and A. Klein-Paste, "Effect of Temperature and Prewetting for Ice Penetration with Sodium Formate," *Transp. Res. Record,* vol. 2674, no. 6, pp. 140-150, 2020, doi: 10.1177/0361198120917974.

[20] H. U. Sajid, D. L. Naik, and R. Kiran, "Improving the ice-melting capacity of traditional deicers," *Construction and Building Materials,* vol. 271, p. 121527, 2021.

[21] A. Klein-Paste and J. Potapova, "Thermal aspects of melting ice with deicer chemicals," *Transp. Res. Record,* vol. 2440, no. 1, pp. 69-75, 2014.

[22] J. Wåhlin and A. Klein-Paste, "The effect of mass diffusion on the rate of chemical ice melting using aqueous solutions," *Cold Regions Science and Technology,* Article vol. 139, pp. 11-21, 2017, doi: 10.1016/j.coldregions.2017.04.001.

[23] J. Wåhlin and A. Klein-Paste, "Ice Melting Rates at− 5° C,− 10° C, and− 15° C Using Chloride Solutions: a Physical Explanation," 2018.

[24] M. Giangi, F. Stella, and T. A. Kowalewski, "Phase change problems with free convection: fixed grid numerical simulation," *Computing and Visualization in Science,* vol. 2, no. 2, pp. 123-130, 1999.

[25] A. Sharma, V. V. Tyagi, C. R. Chen, and D. Buddhi, "Review on thermal energy storage with phase change materials and applications," *Renewable and Sustainable Energy Reviews,* vol. 13, no. 2, pp. 318-345, 2009. [Online]. Available: http://www.sciencedirect.com/science/article/B6VMY-4RCF741-1/2/0314e4fb616b6631bafe70fc8796b008

[26] C. R. Bury and G. A. Parry, "139. The densities of aqueous solutions of potassium acetate and laurate," *Journal of the Chemical Society (Resumed),* 10.1039/JR9350000626 no. 0, pp. 626-628, 1935, doi: 10.1039/JR9350000626.

[27] A.-J. N. Khalifa, "Natural convective heat transfer coefficient–a review: I. Isolated vertical and horizontal surfaces," *Energy conversion and management,* vol. 42, no. 4, pp. 491-504, 2001.

[28] A.S.H.R.A.E, "Fundamentals, 1981," *American Society of Heating, Refrigerating and Air-conditioning Engineers, Atlanta, GA,* 1981.

[29] Ozisik and M. Necati, "Heat transfer: a basic approach," *New York: McGraw-Hill,* vol. 780, 1985.